Electron-driven C_2-symmetric Dirac semimetal uncovered in $Ca_3Ru_2O_7$

M. Horio,[1] Q. Wang,[1] V. Granata,[2,3] K. P. Kramer,[1] Y. Sassa,[4] S. Jöhr,[1] D. Sutter,[1] A. Bold,[1] L. Das,[1] Y. Xu,[1] R. Frison,[5] R. Fittipaldi,[2,3] T. K. Kim,[6] C. Cacho,[6] J. E. Rault,[7] P. Le Fèvre,[7] F. Bertran,[7] N. C. Plumb,[8] M. Shi,[8] A. Vecchione,[2,3] M. H. Fischer,[1] and J. Chang[1]

[1] *Physik-Institut, Universität Zürich, Winterthurerstrasse 190, CH-8057 Zürich, Switzerland*
[2] *CNR-SPIN, I-84084 Fisciano, Salerno, Italy*
[3] *Dipartimento di Fisica "E.R. Caianiello", Università di Salerno, I-84084 Fisciano, Salerno, Italy*
[4] *Department of Physics, Chalmers University of Technology, SE-412 96 Göteborg, Sweden*
[5] *Center for X-ray Analytics, Swiss Federal Laboratories for Materials Science and Technology (Empa), Überlandstrasse 129, CH-8600 Dübendorf, Switzerland*
[6] *Diamond Light Source, Harwell Campus, Didcot, OX11 0DE, United Kingdom*
[7] *Synchrotron SOLEIL, Saint-Aubin-BP 48, F-91192 Gif sur Yvette, France*
[8] *Swiss Light Source, Paul Scherrer Institut, CH-5232 Villigen PSI, Switzerland*

Two-dimensional semimetals have been the center of intensified investigations since the realization of graphene. In particular, the design of Dirac and Weyl semimetals has been scrutinized. Typically, Dirac metals emerge from crystal-field environments captured by density functional theory (DFT). Here, we show by angle-resolved photoemission spectroscopy (ARPES) how a rotational symmetry broken massive Dirac semimetal is realized in $Ca_3Ru_2O_7$. This Dirac semimetal emerges in a two-stage electronic transition driven by electron correlations beyond the DFT paradigm. The Dirac point and band velocity is consistent with constraints set by quantum oscillation, thermodynamic and transport experiments. Our results hence advance the understanding of the peculiar fermiology found in $Ca_3Ru_2O_7$. As the two-stage Fermi surface transition preserves the Brillouin zone, translational broken symmetries are excluded. The mechanism and symmetry breaking elements underlying the electronic reconstruction thus remain to be identified. This situation resembles URu_2Si_2 that also undergoes an electronic transition without an identifiable symmetry breaking. As such our study positions $Ca_3Ru_2O_7$ as another prominent hidden order parameter problem.

Introduction:
Giant diamagnetic responses found in graphite [1] and graphene [2, 3] are directly linked to the "light" effective mass of Dirac fermions [4]. The observation of an even larger diamagnetic response upon application of electric current to Mott insulating Ca_2RuO_4 therefore came as a surprise [5], even though it was known that electrical current induces remetallization [6]. To account for the diamagnetic response, the existence of a light-mass semimetal driven by electron correlations has been put forward [5]. Experimentally it is, however, challenging to confirm the existence of such a semimetallic state on the verge of the Mott transition. First, the current-induced semimetal is difficult to realize at temperature scales relevant for quantum oscillations. Second, application of current is not easily compatible with high-resolution angle-resolved photoemission spectroscopy (ARPES) experiments. The mechanism of the current-induced diamagnetism and the Mott-insulator-to-semimetal transition therefore remains unexplained.

The Mott insulating transition ($T_c \approx 350$ K [7, 8]) of Ca_2RuO_4 is associated with a pronounced c-axis lattice compression [9, 10], that drives the d_{xy} orbital channel to band insulating (fully occupied) whereas the resulting half-filled d_{xz} and d_{yz} sectors go Mott insulating [11, 12]. A similar but much less pronounced c-axis lattice compression without a space-group change [$Bb2_1m$ (No. 36)] is found in the orthorhombic bi-layer system $Ca_3Ru_2O_7$ at $T_s = 48$ K [13]. A-type antiferromagnetic (AFM) order setting in at $T_N = 56$ K [13] also undergoes a spin reorientation across this temperature: Magnetic moments flip from the orthorhombic a-axis (AFM-a at $T > T_s$) to the b-axis (AFM-b at $T < T_s$) direction [14, 15]. Upon the c-axis compression, the out-of-plane resistivity ρ_c increases by an order of magnitude whereas the in-plane resistivity is much less impacted [16]. This electronically two-dimensional state of $Ca_3Ru_2O_7$ displays interesting semimetal-like properties at low temperature including large magnetoresistance [17]. An extremely small quasiparticle residue Z [18] and an insulating ground state reached by only 0.5% of Ti substitution for Ru [19] indicate its close proximity to a Mott insulating state. Although diamagnetism has only been observed in Ti substituted compounds under dc current [20], $Ca_3Ru_2O_7$ thus stands as an intriguing system near the boundary between a semimetal and Mott insulator. Quantum oscillation experiments have revealed the existence of small Fermi surface pockets [17, 21, 22] while an ARPES study reported boomerang-like Fermi arcs [18]. The fact that these observations are not directly reconcilable suggests that the electronic structure of $Ca_3Ru_2O_7$ and the symmetry breaking remain unsettled.

More recently, transport experiments have put forward evidences of in-plane anisotropic electronic susceptibility [22]. The problem of understanding the electronic properties of $Ca_3Ru_2O_7$ therefore connects to a broader topic of nematicity found in t_{2g} multi-orbital systems [23–28]. Magnetic-field-induced nematicity has been re-

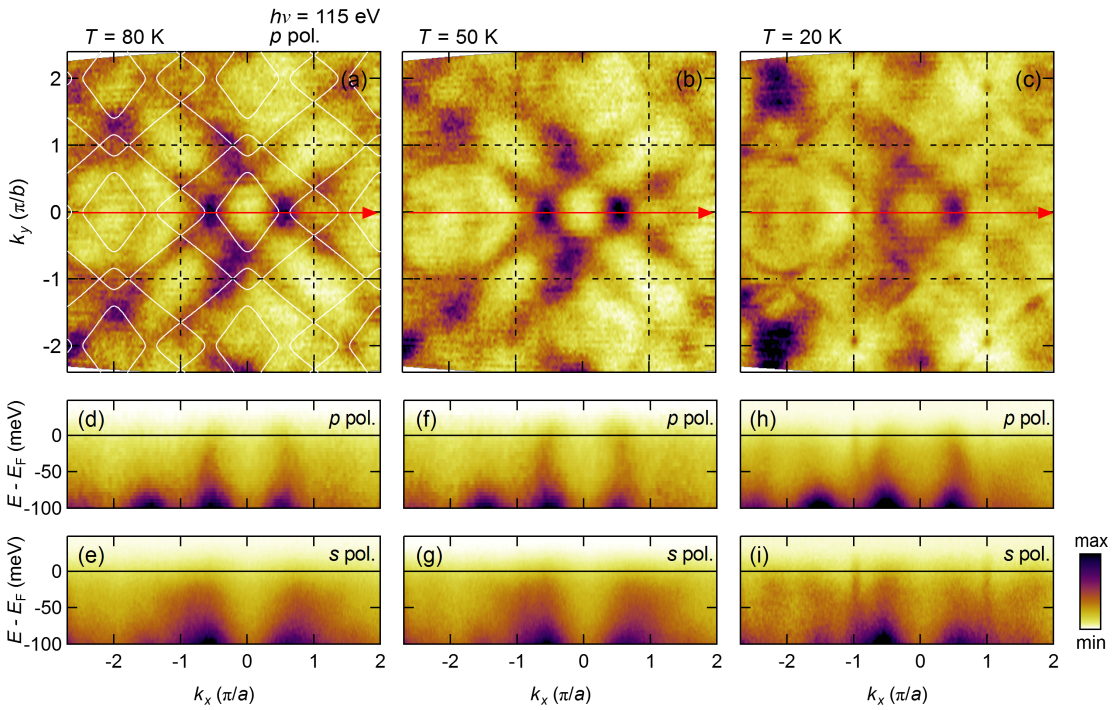

FIG. 1. **Fermi-surface reconstruction in $Ca_3Ru_2O_7$.** (a)–(c) Fermi surface maps taken at $T = 80$, 50, and 20 K, respectively. The photoelectron intensity has been integrated within $E_F \pm 20$ meV. Superimposed in (a) are Fermi surfaces from a tight-binding model of Ru t_{2g} orbitals [31]. (d)–(i) Energy distribution maps measured at $T = 80$ K along the cut indicated in (a) with p and s polarized light, respectively.

ported in the context of $Sr_3Ru_2O_7$ [23, 29]. It is also an active theme for superconducting iron pnictide and chalcogenide systems. Nematic orders have for example been identified in systems such as $BaFe_{2-x}Co_xAs_2$ [24, 25, 30] and FeSe [26–28]. Common to these systems ($Sr_3Ru_2O_7$, $BaFe_{2-x}Co_xAs_2$ and FeSe) is that the nematicity connects intimately with spin-density-wave order/fluctuations. Since $Ca_3Ru_2O_7$ is ordering with both ferromagnetic (in-plane) and AFM (out-of-plane) couplings, it is magnetically different from the other t_{2g} systems displaying nematic tendencies. It is therefore interesting to explore the in-plane anisotropy of $Ca_3Ru_2O_7$.

Here we show by direct ARPES experiments that $Ca_3Ru_2O_7$ is an electronically driven Dirac semimetal at low temperature. We reveal the complete set of anisotropic Fermi surfaces: A small electron pocket formed by massive Dirac fermions is found at the short-axis orthorhombic zone boundary whereas boomerang-like FS sheets are found in vicinity to the long-axis zone boundary. The temperature evolution into this C_4-broken state appears to have two stages. Electronic reconstruction appears first below $T_{s1} = 48$ K and eventually the system settles into the low-temperature structure below $T_{s2} = 30$ K. Throughout this temperature evolution, no signature of Brillouin-zone folding is identified, excluding any $Q \neq 0$ density-wave/orbital order as the origin of the phase transition at $T_{s1} = 48$ K. Our study thus demonstrates an intriguing case where electron interactions, without apparent symmetry breaking, induces a C_2-symmetric Dirac semi-metallic state starting from a correlated metal.

Methods:

High quality single crystals of $Ca_3Ru_2O_7$ were grown by floating zone technique [16]. The electronic transition at $T_{s1} = 48$ K was checked by thermopower measurements (see Supplementary Fig. 1 [31]) and found in agreement with existing literatures [22, 32]. Detwinning of orthorhombic domains was achieved with a thermomechanical device [33] and monitored by polarized light microscopy. The resulting mono domain constitutes 99% (or more) of the sample volume according to x-ray diffraction measurements (see Supplementary Fig. 2 [31]).

Angle-resolved photoemission spectroscopy (ARPES) experiments were carried out at the SIS [34], CASSIOPEE, and I05 [35] beamlines of the Swiss Light Source (SLS), SOLEIL synchrotron, and Diamond Light Source, respectively. Pristine surfaces were obtained by top-post cleaving at $T > T_{s1}$ (80 K). Incident photons with various photon energies, ranging from $h\nu = 31$ to 115 eV, were used for the measurements. Consistent

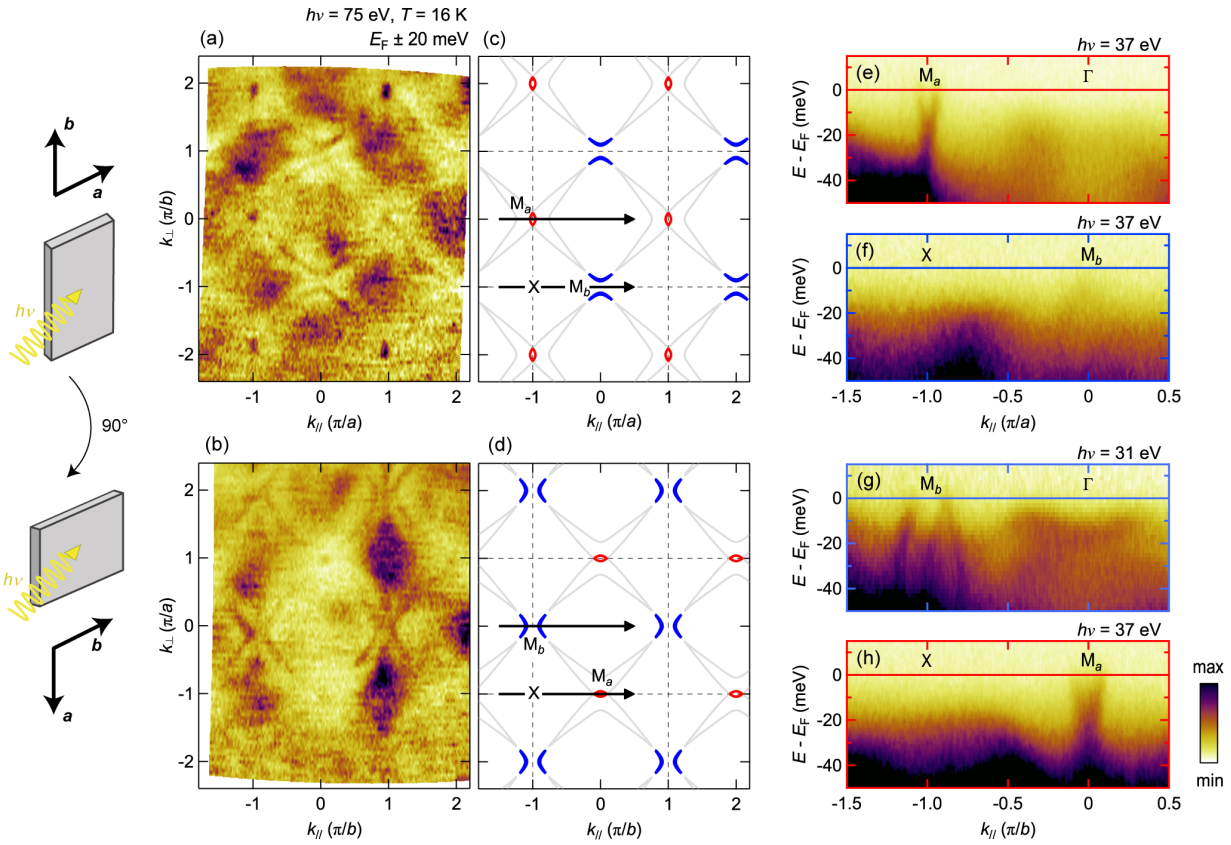

FIG. 2. **Breaking of four-fold rotational symmetry.** (a),(b) Fermi surface maps recorded at $T = 16$ K ($h\nu = 75$ eV) for two sample azimuthal angles that are 90° apart as indicated in the schematics. The azimuthal angle rotation was operated *in-situ* and hence the sample surface is identical. $k_\parallel$ ($k_\perp$) represents momentum parallel (perpendicular) to the electron-analyser slit. The spectral intensity was integrated within $E_F \pm 20$ meV. (c),(d) Fermi surfaces from the tight-binding model [31]. The sheets not observed in the experiment are indicated in gray. (e)–(h) Energy distribution maps along M_a–Γ, X–M_b, M_b–Γ, and X–M_a as shown in panels (c) and (d). The energy distribution maps were recorded at $h\nu = 37$ eV except for (g) where $h\nu = 31$ eV incident light was used. The band structure along M_a–Γ (X–M_a) and M_b–Γ (X–M_b) is inequivalent.

results were obtained on different crystals and upon cooling and heating through the critical temperature $T_{s1} = 48$ K below which the electronic structure is reconstructed. ARPES data are presented using orthorhombic notation with lattice parameters $a = 5.37$ Å and $b = 5.54$ Å.

Results:

Normal state: The Fermi surface and low-energy electronic structure of the $Ca_3Ru_2O_7$ normal state – above the Néel temperature $T_N = 56$ K – are presented in Figs. 1(a), (d), and (e). The orthorhombic zone boundary is indicated by black dashed lines in Fig. 1(a). All quasiparticle dispersions are broad irrespective of whether linear horizontal or vertical polarized light is used. This fact indicates a strongly correlated electronic state. Part of the Fermi surface consists of quasi-one-dimensional sectors running diagonally through the orthorhombic Brillouin zone. This structure remains essentially unchanged across the Néel transition $T_N = 56$ K [see Figs. 1(b), (f), and (g)].

Rotational symmetry breaking: Across the structural transition at $T_{s1} = 48$ K, however, the electronic structure undergoes a dramatic reconstruction. This is evidenced by the emergence of a fast dispersing band and a tiny Fermi surface around $M_a = (\pm\pi/a, 0)$ – see Figs. 1(c), (h), and (i). Remarkably, this small Fermi surface sheet is absent at $M_b = (0, \pm\pi/b)$. Instead, as previously reported [18], boomerang-like Fermi surface sheets are found around the M_b point. Therefore, while the high temperature ($T > T_{s1}$) Fermi surface is quasi four-fold symmetric, the low-temperature structure seems to break C_4 symmetry.

To exclude the possibility that this C_2 symmetry is an artifact of photoionization matrix-element effects, we follow a standard measurement protocol [24, 36]. That is to carry out Fermi surface mappings with azimuthal angles differing from each other by 90° [see Figs. 2(a)

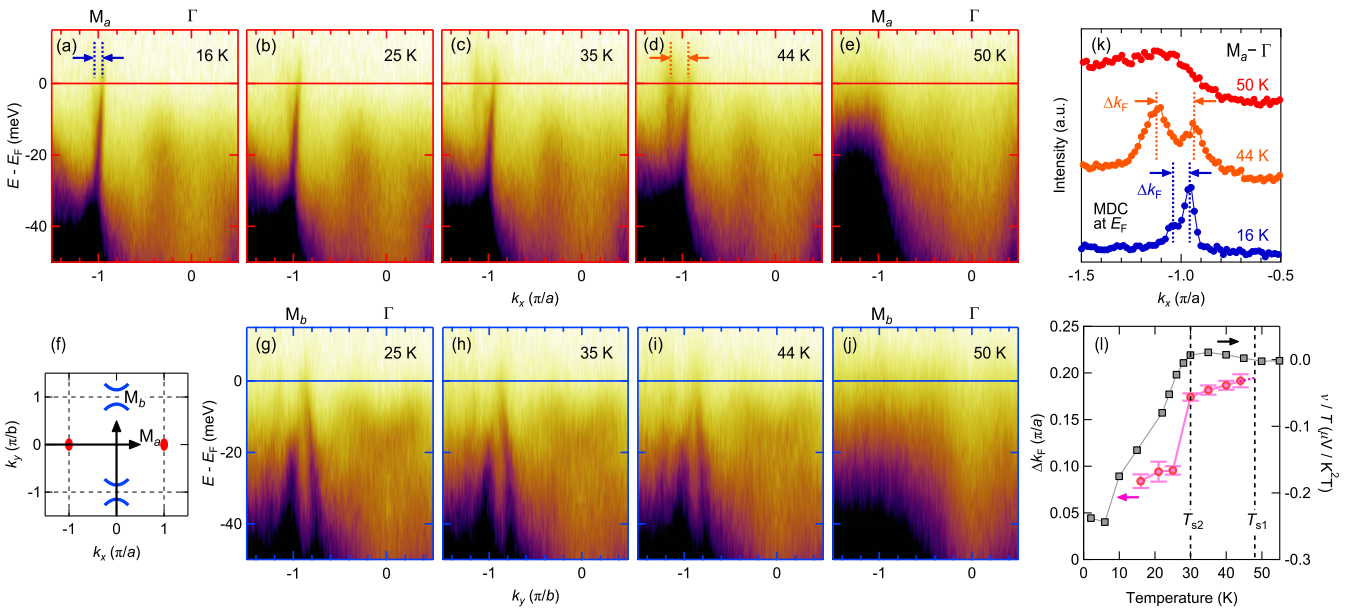

FIG. 3. **Two-stage temperature evolution of the band structure.** (a)–(j) Energy distribution maps along M_a–Γ (top panels) and M_b–Γ (bottom panels) for temperatures as indicated. (f) Schematics of the Fermi surface and the high-symmetry cuts used in (a)–(e) and (g)–(j). (k) MDCs at E_F (integrated within ±3 meV) extracted from EDMs in (a), (d), and (e). Clear difference in the peak separation, Δk_F, is found between 16 K and 44 K. (l) Δk_F plotted as a function of temperature. The error bars represent 3σ of the fitting with σ being the standard deviation. For comparison, the Nernst coefficient ν [22] is plotted as ν/T versus T. Both experiments suggest an electronic transformation across $T = 30$ K.

and (b)]. This azimuthal rotation was done *in-situ* and hence the Fermi surface maps in Figs. 2(a) and (b) were obtained on the same surface. Here, $k_\parallel$ ($k_\perp$) on the horizontal (vertical) axis represents the momentum parallel (perpendicular) to the electron-analyser slit. The electronic structure with a tiny Fermi pocket around the M_a point and boomerang-like features near M_b tracks the azimuthal rotation – see Figs. 2(a)–(d). The C_2 symmetric electronic structure is also revealed by the band dispersions. Along the M_a–Γ and M_b–Γ directions, the band curvature around M_a and M_b are clearly different [Figs. 2(e) and (g)]. An electron pocket is formed around M_a whereas two hole-like pockets are found on each side of M_b. In a similar fashion, dispersions along the M_a–X and M_b–X directions are inequivalent [Figs. 2(f) and (h)]. Electron-like band curvature is found around M_a whereas no Fermi crossing is observed along M_b–X. These results allow us to exclude matrix element effects as the source of the observed rotational-symmetry breaking and prove it to be an intrinsic property of $Ca_3Ru_2O_7$.

Two-stage Fermi surface reconstruction: By tracking the temperature dependence of the band structure, two electronic temperature scales are revealed. The electronic band structure along M_a–Γ and M_b–Γ is shown for temperatures spanning from 16 K to 50 K. Above $T_{s1} = 48$ K [Figs. 3(e), (j) and Fig. 1], all the bands appear with broad line-shapes. Once cooled below T_{s1}, well-defined bands around the M_a and M_b points emerge [see Figs. 3(d), (i), and (k)]. A gapped electron-like band also appears around the Γ point. The band structures around M_a and M_b are inequivalent not only in terms of curvature but also in terms of temperature dependence. The M_a–Γ band dispersion is temperature dependent whereas the corresponding structure around M_b is virtually insensitive to temperature. Examining the momentum distribution curve (MDC) at E_F in Fig. 3(k), at 44 K one finds that the two intensity maxima are not symmetrically positioned around M_a. To quantify the temperature evolution, we define Δk_F as the reciprocal-space distance between these two intensity maxima. As a function of temperature, Δk_F drops by a factor of two across $T_{s2} = 30$ K. This electronic transformation is also visible in the band dispersion along the M_a–Γ direction [see Figs. 3(b) and (c)]. In fact, T_{s2} coincides with the temperature T^* where a sudden decrease of ν/T (ν: Nernst coefficient) was found [22] [see Fig. 3(l)]. At base temperature, the two peak maxima are within the experimental error bars centered around the M_a point. The low-temperature Fermi surface thus emerges as a result of two reconstructions. First below $T_{s1} = 48$ K, a fast dispersing band appears around M_a and M_b. The observed electronic dispersions suggest that rotational symmetry is breaking already across T_{s1}. Next, the band dispersion along the M_a–Γ direction undergoes a second

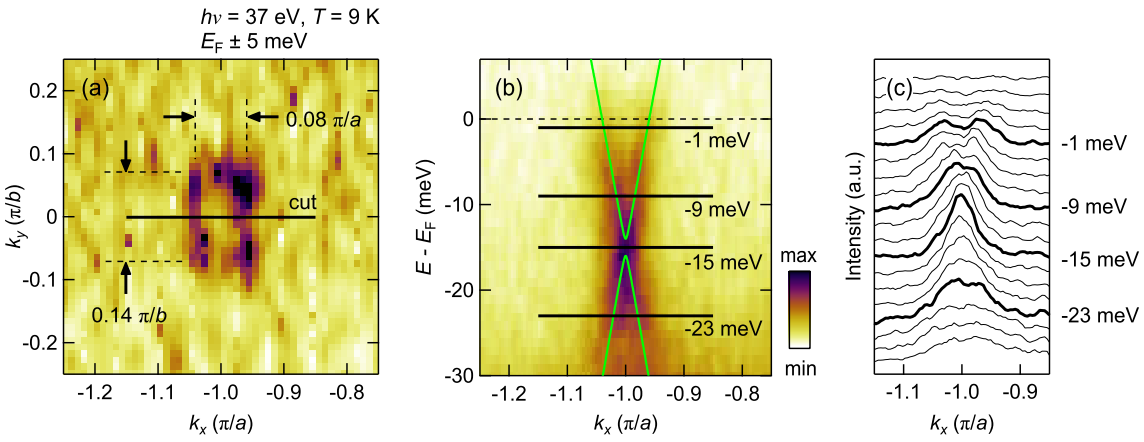

FIG. 4. **Dirac cone structure in $Ca_3Ru_2O_7$** (a) High-resolution Fermi surface map around the M_a point. (b) Energy distribution map along the M_a–Γ direction evidencing a Dirac cone structure. Crystal/magnetic symmetry imposes a finite mass as illustrated by green dispersions reproduced by the tight-binding model [31]. (c) MDCs, extracted from (b), at binding energies as indicated.

transformation across $T_{s2} = 30$ K.

Low-temperature electronic structure: We now examine the low-temperature ($T < T_{s2}$) electronic structure. Except for the structures around the M_a and M_b points, all bands are gapped as evident from Figs. 2(e)–(h). Around the M_b point, two hole-like bands – forming an M-shaped structure – is found [Fig. 2(g)]. While the hole-like band touches E_F along the M_b–Γ direction [Fig. 2(g)], the band top sinks below E_F upon moving away from it (See Supplementary Fig. 3 [31]) consistent with a previous report [18]. The boomerang-like feature thus forms a closed hole-like Fermi surface.

Around the M_a point, the electron-like Fermi surface pocket is revealed by a high-resolution map in Fig. 4(a). The topology of this electron pocket is elliptical with $k_F^a = 0.04\pi/a$ and $k_F^b = 0.07\pi/b$ along the M_a–Γ and M_a–X directions, respectively. The Fermi surface area $A_{FS} = \pi k_F^a k_F^b$ corresponds to approximately 0.23% of the orthorhombic Brillouinz zone. Inspecting the band dispersion along the M_a–Γ direction reveals a Dirac-cone structure with the Dirac point placed about $E_D = 15$ meV below E_F [Fig. 4(b)]. The two-peak MDC profile found at E_F merges into a single peak at E_D and then splits again below E_D [see Fig. 4(c)]. From this MDC analysis, a linearized Fermi velocity of $v_F^a = 0.62$ eVÅ (95 km/s) and $v_F^b = 0.37$ eVÅ (57 km/s) is estimated. Our results thus suggest that $Ca_3Ru_2O_7$ at low temperatures is a highly anisotropic Dirac semimetal.

Discussion:
Let us compare the Fermi surface structure observed here with quantum oscillation experiments. Using the Onsager relation [37], the Fermi surface areas are directly linked to the quantum oscillation frequencies $F = \Phi_0 A_{FS}/(2\pi^2)$ where Φ is the flux quantum. The low-temperature electron pocket around M_a corresponds to $F = 34$ T in excellent agreement with observed quantum oscillation frequencies 28–43 T [17, 21, 22]. The hole-like boomerang structure comprises a Fermi surface area that is too small to be quantified accurately by our ARPES experiments. However, it should produce a low-frequency quantum oscillation. Indeed, a frequency corresponding to 0.07% of the Brillouin zone or about 1/3 of the electron pocket has been reported [21]. It is therefore conceivable that the electron- and hole- Fermi pockets reported here are those responsible for the quantum oscillations. Our ARPES work unveils the band curvature and position of these pockets within the Brillouin zone.

As the electron pocket is resolved clearly by both the ARPES and quantum oscillation experiments, a direct comparison of the effective electronic mass $m^* = \frac{\hbar^2}{2\pi}\frac{\partial A_{FS}}{\partial \varepsilon}$ is possible [38, 39]. Analysis of the ∼ 35 T quantum-oscillation frequency yielded $m_e^* = 0.6m_e$ [17], where m_e is the electron mass. Assuming a parabolic band dispersion $m_e^* = \hbar^2 k_F^a k_F^b/2\varepsilon_F$ where $\varepsilon_F = 15$ meV is the Fermi energy, the effective mass $m_e^* = 0.25m_e$ is significantly lower than what has been inferred from quantum-oscillation experiments. If, however, a linear band dispersion $E_k = v_F k$ is assumed, much better agreement $m_e^* = \varepsilon_F/v_F^a v_F^b = A_{FS}/\pi\varepsilon_F = 0.49m_e$ is obtained. This fact reinforces the interpretation of Dirac fermions around M_a. The boomerang band along Γ–M_b has comparable Fermi velocity to that of the electron pocket along Γ–M_a. However, the Fermi energy is estimated to be as small as ∼ 5 meV from linear extrapolation of the M-shaped band dispersion. Since the hole pocket is about 3 times smaller than the electron

sheet, we estimate the hole-like carriers to have an effective mass of $m_h^* = 0.49m_e$. With two hole and one electron pocket per Brillouin zone, a Sommerfeld constant of $\gamma \approx 2.1$ mJ/(mol K^2) is found. Here, we assumed two-dimensional band dispersions without bi-layer splitting. In addition, spin polarization within the RuO_2 plane was employed to treat the A-type AFM order. As the estimate is in reasonable agreement with the value $\gamma \approx 2.8$–3.4 mJ/(mol K^2) obtained by specific heat experiments [16, 17], we conclude that the entire/complete bulk Fermi surface has been revealed.

The two-stage transformation of the electronic structure has a clear impact on all transport coefficients. A remarkable increase of in- and out-of-plane resistivity appears across $T_{s1} = 48$ K [16, 17]. Simultaneously, the Seebeck coefficient changes sign going from weak positive to large negative values across T_{s1} [22]. Although less sharp, the Hall coefficient also changes sign (from positive to negative) across T_{s1}. While the Hall coefficient takes increasingly large negative values [22, 40], the Seebeck coefficient displays a complicated temperature dependence that in addition is different along the a and b directions [22]. This is a typical signature of ambipolar transport behaviour where both electron- and hole-like carriers are contributing [41]. Furthermore, the low-temperature Hall coefficient R_H that ranges between -0.5×10^{-7} m^3/C and -1.4×10^{-7} m^3/C [17, 22, 40] cannot be explained by the electron pocket that alone should generate $R_H = -1/(n_e e) = -8.0 \times 10^{-7}$ m^3/C. Using the combined ARPES and quantum-oscillation knowledge that $n_e = 7.8\times10^{18}$ cm^{-3} and $n_h \approx 2\times n_e/3$, a two band model [42] yields $R_H = (2\alpha^2/3{-}1)/(n_e e)(2\alpha/3{+}1)^2$ where $\alpha = \mu_h/\mu_e$ is the mobility ratio between electrons and holes. The exact experimental values of $R_H(T = 0)$ imply that $\mu_h \approx 0.9$–$1.1 \times\mu_e$ and $\mu_e \approx |R_H|/\rho_{xx} = 0.1$ T^{-1}. We thus infer that in the $T \to 0$ limit electron- and hole-like carriers have comparable mobility that in turn generate the ambipolar transport properties.

Having established the existence of small electron pockets with linear dispersion around the M_a point, a question arises whether these excitations are massless Dirac fermions or whether they posses a finite mass at M_a. While the question cannot be definitively answered from the experimental data due to the finite energy resolution, we discuss here implications from the crystal symmetry. $Ca_3Ru_2O_7$ has the space group $Bb2_1m$ (No. 36) [13]. For our purpose, it is sufficient to focus on a single bi-layer. The point group of such a bi-layer is C_{2v} with a mirror plane between the two layers, as well as a glide plane perpendicular to the mirror and a two-fold screw axis along the crystalline b axis (the longer in-plane axis). Together with time-reversal symmetry (TRS) in the paramagnetic state, this imposes a Kramer's degeneracy along M_b–X in the Brillouin zone. Futhermore, TRS imposes Kramer's pairs at the M_a and Γ point.

When TRS is broken in the A-type AFM phase [14], the generating point group of the bi-layer is reduced to C_{2v} (C_s) for the AFM-a phase and C_{2v} (C_2) for the AFM-b phase. Here, the notation $\mathcal{G}$ ($\mathcal{G}'$) denotes the generating point group $\mathcal{G}$ with $\mathcal{G}'$ the subgroup of elements that do not have to be combined with TRS. While the Kramer's degeneracy is preserved along M_b–X, the one at the M_a and Γ point is lifted. The Dirac fermions at M_a thus possess a finite mass as schematically illustrated in Fig. 4(b).

We can reproduce key features of the low-temperature semi-metallic band structure employing a tight-binding model of the Ru t_{2g} orbitals [31]. Given the "one-dimensional" nature of the high-temperature ($T > 48$ K) Fermi surface, we restrict our model to the Ru d_{xz} and d_{yz} orbitals in an effective single-layer model. Such a model faithfully reproduces the Fermi surface in the normal state as illustrated by Fig. 1(a). Importantly, a rigid band shift, as expected due to the c-axis compression at T_{s1} [13], yields elliptical electron pockets with linear dispersion around the M_a point and a hole-like boomerang structure around the M_b point [Figs. 2(c) and (d)]. Finally, the Brillouin-zone folding due to the screw-axis opens a gap at the M_a point [see Fig. 4(b)]. While our tight-binding model based on the Ru t_{2g} orbitals is too simplistic to capture all the features and does not include the actual electronic instability, it reproduces the most important features of both the high- and low-temperature dispersions. We thus conclude that the origin of the low-temperature pockets are due to the d_{xz} and d_{yz} Ru orbitals.

Conclusions & Outlook:

In summary, we have revealed the low-temperature electronic transformation of $Ca_3Ru_2O_7$. Across $T = 48$ K the system reconstructs from a strongly correlated metal into a C_2-symmetric Dirac semimetal. The ground state electronic structure consists of a Dirac cone forming an elliptical electron pocket around the short-axis orthorhombic zone boundary. By contrast, along the long axis a hole-like Dirac cone constitutes a boomerang shaped Fermi surface. This Fermi surface structure and the observed band velocities are consistent with the sheet areas and electronic masses derived from quantum oscillation experiments. Thermodynamic measurements of the density of states are also consistent with the identified structure. Finally, it is shown that the low-temperature state emerges in two steps. First, the Fermi surface reconstructs at $T_{s1} = 48$ K. A second transformation along the short-orthorhombic axis settles the ground state structure below $T_{s2} = 30$ K. The Fermi surface transformation and the low-temperature structure is described with a simple tight-binding model containing only d_{xz}/d_{yz} orbitals. Overall, the identified C_2-symmetric Dirac semimetallic structure provides an understanding of the fermionic properties observed by quantum oscilla-

tion, specific heat, and electronic transport experiments.

In outlook, the state of matter that makes the C_2-symmetric Dirac semimetal energetically favorable should be scrutinized. In Ca_2RuO_4, a Mott insulating state offers an energetically favorable ground state, through a c-axis compressive crystal field environment [9, 11, 12]. Although much weaker in $Ca_3Ru_2O_7$, a similar seemingly disfavorable c-axis compressive crystal field environment occurs across the critical temperature for the Fermi surface reconstruction [13]. A fundamental question is what triggers the sudden change of crystal field environment that in turn induces the C_2-symmetric Dirac semimetal. Specific heat suggests that the crystal field changes through a phase transition involving a large entropy change [16]. Within a Landau paradigm, this implies symmetry breaking. It appears unlikely that the spin reorientation, that changes slightly the point symmetry group, is responsible for the large entropy change and the Fermi surface reconstruction. As the Fermi surface reconstruction preserves the orthorhombic lattice Brillouin zone, density waves (charge, spin or orbital) breaking lattice translational symmetry can be excluded. As such, $Ca_3Ru_2O_7$ resembles the hidden order problem of URu_2Si_2 [43] where crystal field environment [44] and Fermi surface reconstruction [45] occurs without an identifiable symmetry breaking. Recently, it has been proposed that $Ca_3Ru_2O_7$ hosts magnetic anapole order [46, 47]. A direct resonant x-ray diffraction confirmation of anapole order would be of great interest. Finally, $Ca_3Ru_2O_7$ could be an example of physics going beyond the Landau paradigm [48, 49]. If so, the origin of the here reported Fermi surface reconstruction is rooted in topology rather than symmetry breaking.

Acknowledgements:
We thank M. Hoesch for fruitful discussions. M.H., Q.W., K.P.K., D.S., Y.X., and J.C. acknowledge support by the Swiss National Science Foundation. Y.S. is funded by the Swedish Research Council (VR) with a Starting Grant (Dnr. 2017-05078). ARPES measurements were carried out at the SIS, CASSIOPEE, and I05 beamlines of the Swiss Light Source, SOLEIL synchrotron, and Diamond Light Source, respectively. We acknowledge Diamond Light Source for time at beamline I05 under proposal SI20259.

[1] M. P. Sharma, L. G. Johnson, and J. W. McClure, Phys. Rev. B **9**, 2467 (1974).
[2] Z. Li, L. Chen, S. Meng, L. Guo, J. Huang, Y. Liu, W. Wang, and X. Chen, Phys. Rev. B **91**, 094429 (2015).
[3] M. Sepioni, R. R. Nair, S. Rablen, J. Narayanan, F. Tuna, R. Winpenny, A. K. Geim, and I. V. Grigorieva, Phys. Rev. Lett. **105**, 207205 (2010).
[4] H. Fukuyama, Prog. Theor. Phys. **45**, 704 (1971).
[5] C. Sow, S. Yonezawa, S. Kitamura, T. Oka, K. Kuroki, F. Nakamura, and Y. Maeno, Science **358**, 1084 (2017).
[6] F. Nakamura, M. Sakaki, Y. Yamanaka, S. Tamaru, T. Suzuki, and Y. Maeno, Sci. Rep. **3**, 2536 (2013).
[7] S. Nakatsuji, S.-i. Ikeda, and Y. Maeno, J. Phys. Soc. Jpn. **66**, 1868 (1997).
[8] S. Nakatsuji and Y. Maeno, Phys. Rev. Lett. **84**, 2666 (2000).
[9] O. Friedt, M. Braden, G. André, P. Adelmann, S. Nakatsuji, and Y. Maeno, Phys. Rev. B **63**, 174432 (2001).
[10] Q. Han and A. Millis, Phys. Rev. Lett. **121**, 067601 (2018).
[11] D. Sutter, C. G. Fatuzzo, S. Moser, M. Kim, R. Fittipaldi, A. Vecchione, V. Granata, Y. Sassa, F. Cossalter, G. Gatti, M. Grioni, H. M. Ronnow, N. C. Plumb, C. E. Matt, M. Shi, M. Hoesch, T. K. Kim, T.-R. Chang, H.-T. Jeng, C. Jozwiak, A. Bostwick, E. Rotenberg, A. Georges, T. Neupert, and J. Chang, Nat. Commun. **8**, 15176 (2017).
[12] L. Das, F. Forte, R. Fittipaldi, C. G. Fatuzzo, V. Granata, O. Ivashko, M. Horio, F. Schindler, M. Dantz, Y. Tseng, D. E. McNally, H. M. Rønnow, W. Wan, N. B. Christensen, J. Pelliciari, P. Olalde-Velasco, N. Kikugawa, T. Neupert, A. Vecchione, T. Schmitt, M. Cuoco, and J. Chang, Phys. Rev. X **8**, 011048 (2018).
[13] Y. Yoshida, S.-I. Ikeda, H. Matsuhata, N. Shirakawa, C. H. Lee, and S. Katano, Phys. Rev. B **72**, 054412 (2005).
[14] W. Bao, Z. Q. Mao, Z. Qu, and J. W. Lynn, Phys. Rev. Lett. **100**, 247203 (2008).
[15] B. Bohnenbuck, I. Zegkinoglou, J. Strempfer, C. Schüßler-Langeheine, C. S. Nelson, P. Leininger, H.-H. Wu, E. Schierle, J. C. Lang, G. Srajer, S. I. Ikeda, Y. Yoshida, K. Iwata, S. Katano, N. Kikugawa, and B. Keimer, Phys. Rev. B **77**, 224412 (2008).
[16] Y. Yoshida, I. Nagai, S.-I. Ikeda, N. Shirakawa, M. Kosaka, and N. Môri, Phys. Rev. B **69**, 220411(R) (2004).
[17] N. Kikugawa, A. Winfried Rost, C. William Hicks, A. John Schofield, and A. Peter Mackenzie, J. Phys. Soc. Jpn. **79**, 024704 (2010).
[18] F. Baumberger, N. J. C. Ingle, N. Kikugawa, M. A. Hossain, W. Meevasana, R. S. Perry, K. M. Shen, D. H. Lu, A. Damascelli, A. Rost, A. P. Mackenzie, Z. Hussain, and Z.-X. Shen, Phys. Rev. Lett. **96**, 107601 (2006).
[19] S. Tsuda, N. Kikugawa, K. Sugii, S. Uji, S. Ueda, M. Nishio, and Y. Maeno, Phys. Rev. B **87**, 241107(R) (2013).
[20] C. Sow, R. Numasaki, G. Mattoni, S. Yonezawa, N. Kikugawa, S. Uji, and Y. Maeno, Phys. Rev. Lett. **122**, 196602 (2019).
[21] G. Cao, L. Balicas, Y. Xin, J. E. Crow, and C. S. Nelson, Phys. Rev. B **67**, 184405 (2003).
[22] H. Xing, L. Wen, C. Shen, J. He, X. Cai, J. Peng, S. Wang, M. Tian, Z.-A. Xu, W. Ku, Z. Mao, and Y. Liu, Phys. Rev. B **97**, 041113(R) (2018).
[23] R. A. Borzi, S. A. Grigera, J. Farrell, R. S. Perry, S. J. S. Lister, S. L. Lee, D. A. Tennant, Y. Maeno, and A. P. Mackenzie, Science **315**, 214 (2007).
[24] M. Yi, D. Lu, J.-H. Chu, J. G. Analytis, A. P. Sorini, A. F. Kemper, B. Moritz, S.-K. Mo, R. G. Moore, M. Hashimoto, W.-S. Lee, Z. Hussain, T. P. Devereaux,

I. R. Fisher, and Z.-X. Shen, Proc. Natl. Acad. Sci. **108**, 6878 (2011).
[25] S. Ishida, M. Nakajima, T. Liang, K. Kihou, C. H. Lee, A. Iyo, H. Eisaki, T. Kakeshita, Y. Tomioka, T. Ito, and S. Uchida, Phys. Rev. Lett. **110**, 207001 (2013).
[26] M. A. Tanatar, A. E. Böhmer, E. I. Timmons, M. Schütt, G. Drachuck, V. Taufour, K. Kothapalli, A. Kreyssig, S. L. Bud'ko, P. C. Canfield, R. M. Fernandes, and R. Prozorov, Phys. Rev. Lett. **117**, 127001 (2016).
[27] T. Shimojima, Y. Suzuki, T. Sonobe, A. Nakamura, M. Sakano, J. Omachi, K. Yoshioka, M. Kuwata-Gonokami, K. Ono, H. Kumigashira, A. E. Böhmer, F. Hardy, T. Wolf, C. Meingast, H. v. Löhneysen, H. Ikeda, and K. Ishizaka, Phys. Rev. B **90**, 121111(R) (2014).
[28] M. D. Watson, T. K. Kim, L. C. Rhodes, M. Eschrig, M. Hoesch, A. A. Haghighirad, and A. I. Coldea, Phys. Rev. B **94**, 201107(R) (2016).
[29] C. Lester, S. Ramos, R. S. Perry, T. P. Croft, R. I. Bewley, T. Guidi, P. Manuel, D. D. Khalyavin, E. M. Forgan, and S. M. Hayden, Nat. Mater. **14**, 373 (2015).
[30] J.-H. Chu, J. G. Analytis, K. De Greve, P. L. McMahon, Z. Islam, Y. Yamamoto, and I. R. Fisher, Science **329**, 824 (2010).
[31] See Supplemental Material for details of the tight-binding model and Supplementary Figures, which includes Refs. 9, 10, 13, 50, and 51.
[32] K. Iwata, M. Kosaka, S. Katano, N. Mri, Y. Yoshida, and N. Shirakawa, J. Magn. Magn. Mater. **310**, 1125 (2007).
[33] Z.-G. Y. E. Burkhardt and H. Schmid, Rev. Sci. Instrum. **66**, 3888 (1995).
[34] U. Flechsig, L. Patthey, and T. Schmidt, AIP Conf. Proc. **705**, 316 (2004).
[35] M. Hoesch, T. K. Kim, P. Dudin, H. Wang, S. Scott, P. Harris, S. Patel, M. Matthews, D. Hawkins, S. G. Alcock, T. Richter, J. J. Mudd, M. Basham, L. Pratt, P. Leicester, E. C. Longhi, A. Tamai, and F. Baumberger, Rev. Sci. Instrum. **88**, 013106 (2017).
[36] M. D. Watson, A. A. Haghighirad, L. C. Rhodes, M. Hoesch, and T. K. Kim, New J. Phys. **19**, 103021 (2017).
[37] S. E. Sebastian and C. Proust, Annu. Rev. Condens. Matter Phys. **6**, 411 (2015).
[38] P. M. C. Rourke, A. F. Bangura, T. M. Benseman, M. Matusiak, J. R. Cooper, A. Carrington, and N. E. Hussey, New J. Phys. **12**, 105009 (2010).
[39] M. Horio, K. Hauser, Y. Sassa, Z. Mingazheva, D. Sutter, K. Kramer, A. Cook, E. Nocerino, O. K. Forslund, O. Tjernberg, M. Kobayashi, A. Chikina, N. B. M. Schröter, J. A. Krieger, T. Schmitt, V. N. Strocov, S. Pyon, T. Takayama, H. Takagi, O. J. Lipscombe, S. M. Hayden, M. Ishikado, H. Eisaki, T. Neupert, M. Månsson, C. E. Matt, and J. Chang, Phys. Rev. Lett. **121**, 077004 (2018).
[40] Y. Yoshida, S.-I. Ikeda, and N. Shirakawa, J. Phys. Soc. Jpn. **76**, 085002 (2007).
[41] R. Bel, K. Behnia, and H. Berger, Phys. Rev. Lett. **91**, 066602 (2003).
[42] P. M. C. Rourke, A. F. Bangura, C. Proust, J. Levallois, N. Doiron-Leyraud, D. LeBoeuf, L. Taillefer, S. Adachi, M. L. Sutherland, and N. E. Hussey, Phys. Rev. B **82**, 020514(R) (2010).
[43] J. A. Mydosh and P. M. Oppeneer, Rev. Mod. Phys. **83**, 1301 (2011).
[44] P. G. Niklowitz, C. Pfleiderer, T. Keller, M. Vojta, Y.-K. Huang, and J. A. Mydosh, Phys. Rev. Lett. **104**, 106406 (2010).
[45] R. Bel, H. Jin, K. Behnia, J. Flouquet, and P. Lejay, Phys. Rev. B **70**, 220501(R) (2004).
[46] F. Thöle and N. A. Spaldin, Phil. Trans. R. Soc. A **376**, 20170450 (2018).
[47] S. W. Lovesey, D. D. Khalyavin, and G. van der Laan, Phys. Rev. B **99**, 134444 (2019).
[48] S. Lee, J. Jung, A. Go, and E.-G. Moon, arXiv:1803.00578 .
[49] S. Gazit, F. F. Assaad, and S. Sachdev, arXiv:1906.11250 .
[50] D. J. Singh and S. Auluck, Phys. Rev. Lett. **96**, 097203 (2006).
[51] A. Georges, L. de' Medici, and J. Mravlje, Annu. Rev. Condens. Matter Phys **4**, 137 (2013).

Supplemental Material

Electron-driven C_2-symmetric Dirac semimetal uncovered in $Ca_3Ru_2O_7$

M. Horio,[1] Q. Wang,[1] V. Granata,[2,3] K. P. Kramer,[1] Y. Sassa,[4] S. Jöhr,[1] D. Sutter,[1] A. Bold,[1] L. Das,[1] Y. Xu,[1] R. Frison,[5] R. Fittipaldi,[2,3] T. K. Kim,[6] C. Cacho,[6] J. E. Rault,[7] P. Le Fèvre,[7] F. Bertran,[7] N. C. Plumb,[8] M. Shi,[8] A. Vecchione,[2,3] M. H. Fischer,[1] and J. Chang[1]

[1] *Physik-Institut, Universität Zürich, Winterthurerstrasse 190, CH-8057 Zürich, Switzerland*
[2] *CNR-SPIN, I-84084 Fisciano, Salerno, Italy*
[3] *Dipartimento di Fisica "E.R. Caianiello", Università di Salerno, I-84084 Fisciano, Salerno, Italy*
[4] *Department of Physics, Chalmers University of Technology, SE-412 96 Göteborg, Sweden*
[5] *Center for X-ray Analytics, Swiss Federal Laboratories for Materials Science and Technology (Empa), Überlandstrasse 129, CH-8600 Dübendorf, Switzerland*
[6] *Diamond Light Source, Harwell Campus, Didcot, OX11 0DE, United Kingdom*
[7] *Synchrotron SOLEIL, Saint-Aubin-BP 48, F-91192 Gif sur Yvette, France*
[8] *Swiss Light Source, Paul Scherrer Institut, CH-5232 Villigen PSI, Switzerland*

I. SUPPLEMENTARY FIGURES

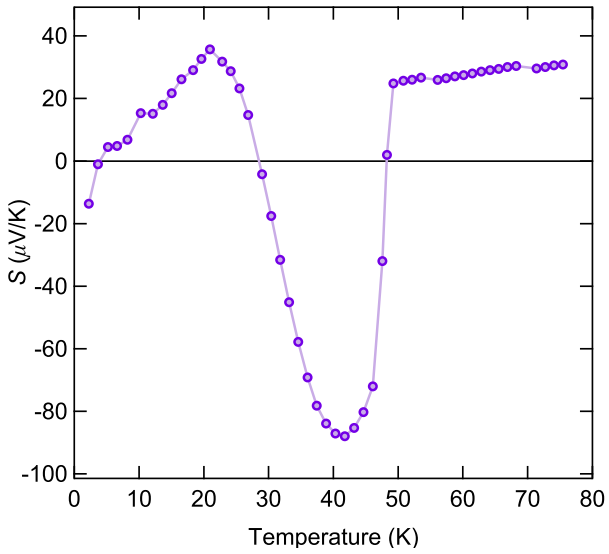

Supplementary Figure 1. **Zero-field thermopower of twinned $Ca_3Ru_2O_7$.**

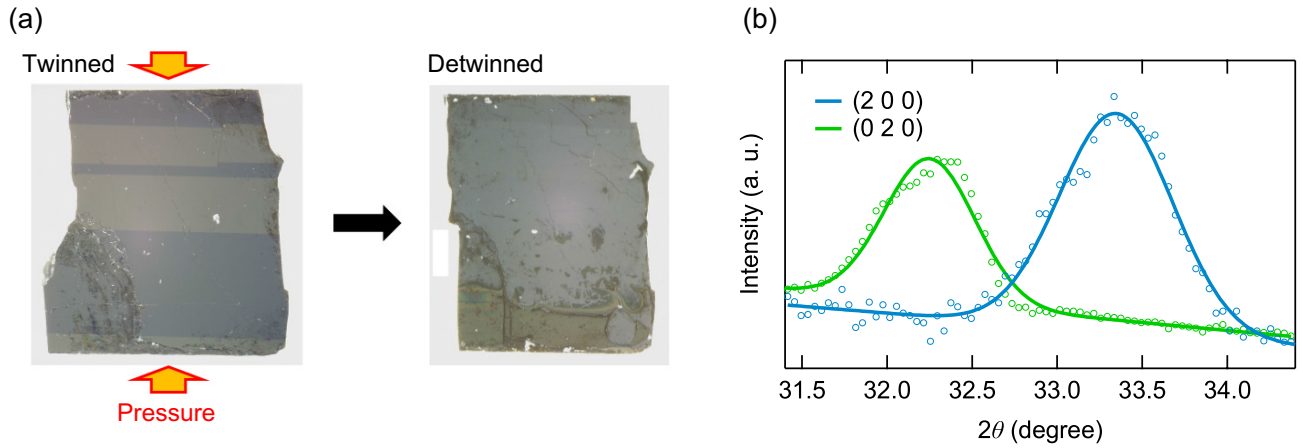

Supplementary Figure 2. **Detwinning of $Ca_3Ru_2O_7$ crystals.** (a) Polarized-light microscope images of a $Ca_3Ru_2O_7$ single crystal before and after detwinning. Domain structure is visualised as a contrast in the sample color. (b) (2 0 0) and (0 2 0) Bragg peaks of the detwinned $Ca_3Ru_2O_7$ obtained from x-ray θ-2θ diffraction measurement. Deduced lattice parameters of $a = 5.37$ Å and $b = 5.54$ Å at room temperature are consistent with the literature values [1]. Selectively observed (2 0 0) and (0 2 0) Bragg peaks indicate the perfection of detwinning.

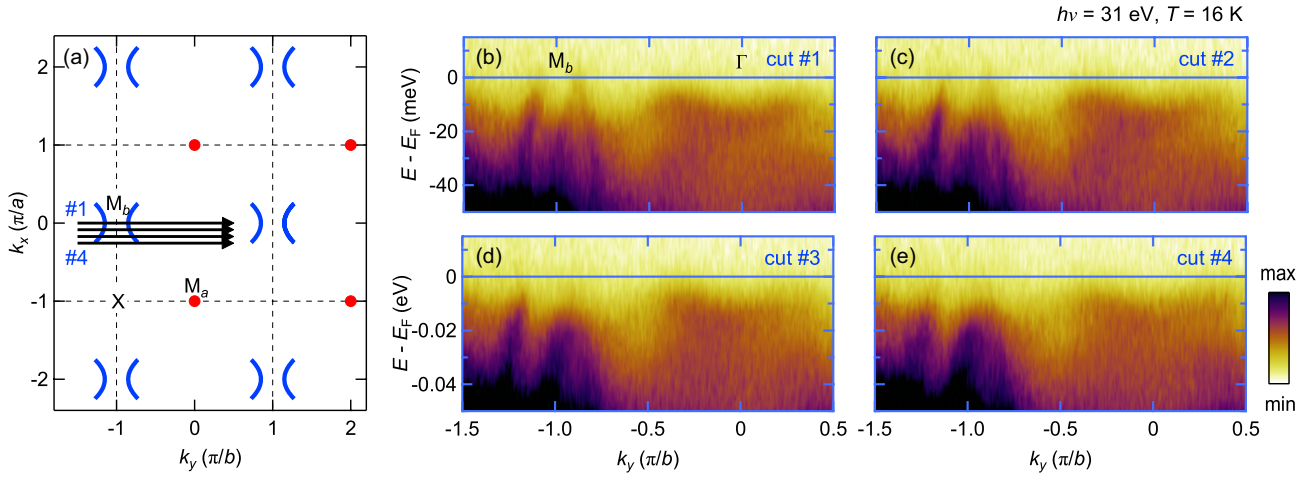

Supplementary Figure 3. **Energy distribution maps around the M_b point.** (a) Schematic Fermi surfaces indicating momentum cut positions. (b)–(e) Energy distribution maps along cuts#1–#4 recorded at $T = 16$ K with incident light of $h\nu = 31$ eV.

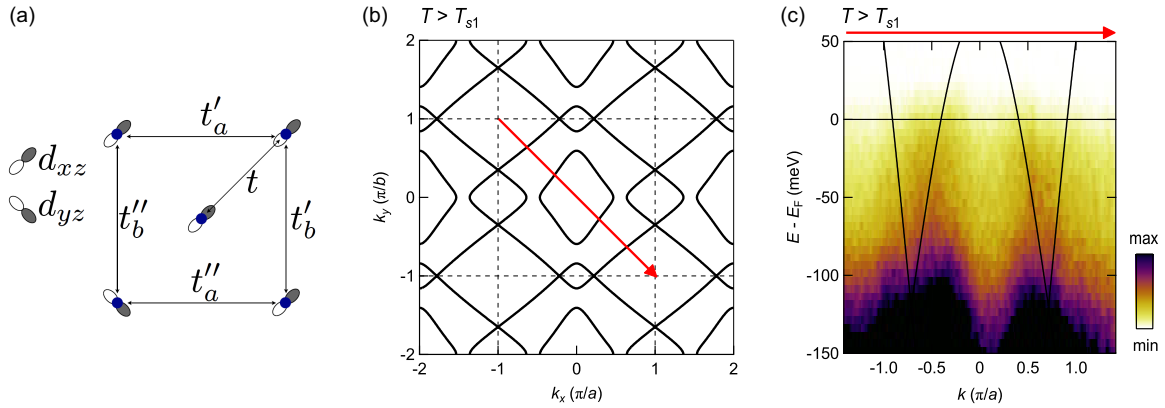

Supplementary Figure 4. **Tight-binding model.** (a) Hopping parameters for the tight-binding model based on the Ru d_{xz} and d_{yz} orbitals. (b) Normal state ($T > T_{s1} = 48$ K) Fermi surface obtained using a tight-binding model with chemical potential $\mu = t$ and hopping parameters $t'_a/t = t'_b/4t = 0.04$ and $t''_a/t = -t''_b/t = 0.32$. This model Fermi surface is plotted in Fig. 1(a) of the main text. (c) ARPES energy distribution map at 80 K along the Brillouin-zone diagonal cut, showing agreement with the tight-binding dispersions with $t = 120$ meV.

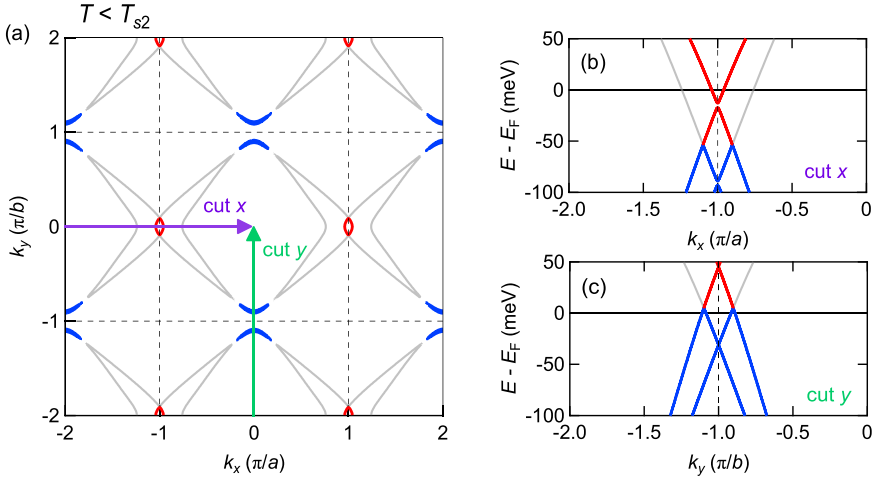

Supplementary Figure 5. **Modeling of the C_2-symmetric Dirac semimetallic structure.** (a) Low-temperature ($T < T_{s2} = 30$ K) Fermi surface obtained from the tight-binding model through justified (see text) change of chemical potential ($\mu/t = 0.19$). All the hopping parameters are kept the same as in the normal state. Red and blue Fermi surface sheets correspond to the observed electron pocket at M_a and boomerang structure around the M_b point. (b) and (c) are the model band dispersion along M_a–Γ and M_b–Γ where $t = 120$ meV has been adjusted to mimic the observed band velocities and the Dirac point. Fermi surfaces and bands not seen in the experiment are plotted in gray.

II. TIGHT-BINDING MODEL

To discuss the origin of the low-temperature semimetallic band structure, we study in the following an effective single-layer tight-binding model. The electronic states close to the Fermi energy derive from the Ru t_{2g} orbitals [2]. Motivated by the strong Hund's coupling which drives the ruthenates towards an orbital selective regime [3] and the experimental observation of the "one-dimensional" nature of the gnormalh state ($T > 48$ K) Fermi surface, we restrict our model to the Ru d_{xz} and d_{yz} orbitals. Specifically, including nearest- and next-to-nearest-neighbor hopping, we start from a d_{yz}- and d_{xz}-based tight-binding Hamiltonian given by

$$\mathcal{H}_{\mathbf{k}} = \begin{pmatrix} \epsilon^{yz}_{\mathbf{k}} - \mu & g_{\mathbf{k}} \\ g_{\mathbf{k}} & \epsilon^{xz}_{\mathbf{k}} - \mu \end{pmatrix}, \tag{1}$$

where

$$\begin{aligned} \epsilon^{xz}_{\mathbf{k}} &= -2t\cos k_X - 2t'_a \cos k_x - 2t'_b \cos k_y, \\ \epsilon^{yz}_{\mathbf{k}} &= -2t\cos k_Y - 2t'_a \cos k_x - 2t'_b \cos k_y, \\ g_{\mathbf{k}} &= -2t''_a \cos k_x - 2t''_b \cos k_y. \end{aligned} \tag{2}$$

Here, $k_X = (k_x - k_y)/2$ and $k_Y = (k_x + k_y)/2$ represent the tetragonal crystal axes, t is a nearest-neighbor hopping parameter, while t'_a (t'_b) and t''_a (t''_b) are intra- and inter- orbital next-nearest-neighbor hopping parameters along the a (b) orthorhombic axes, respectively [see Supplementary Fig. 4(a)]. Further, μ denotes the chemical potential. For simplicity, we omit spin-orbit coupling in our model. Finally, the rotation and tilting of the RuO_6 octahedra leads to a doubling of the unit cell and correspondingly to folded bands. Note that the folding in the a and b direction is not equivalent due to the glide plane and the two-fold screw axis along only the b axis.

The normal state Fermi surface is indeed well reproduced by this simple model as shown in Supplementary Fig. 4(b). Here we have used $t'_a/t = t'_b/4t = 0.04$ and $t''_a/t = -t''_b/t = 0.32$. Finally, we fixed $t = 120$ meV to additionally reproduce the Fermi velocities. Note that we use the low-temperature dispersion for fitting the Fermi velocities, as the high-temperature data is too broad. Nevertheless, the hopping parameters extracted from the low-temperature data is consistent with the dispersion at $T = 80$ K [See Supplementary Fig. 4(c)]. Finally, given the approximately cubic crystal field environment [1], we have set the filling of the d_{xz} and d_{yz} orbitals $n_{xz} = n_{yz} \approx 1/3$, which results in $\mu \approx t$.

Having established a simple model capturing the main feature of the normal state Fermi surface, we use this model to describe the Fermi surface below T_{s1} and the low-temperature band structure. We can reconstruct the most salient observations of the low-temperature band structure, namely an elliptical electron pocket around the M_a point and a hole-like boomerang structure around the M_b point [Supplementary Fig. 5(a)] by only changing the chemical potential ($\mu/t = 0.19$). Importantly, the model correctly exhibits an approximately linear band dispersion close to the Fermi energy [Supplementary Figs. 5(b) and (c)], which is again consistent with the experimentally observed structure.

The change to the chemical potential in the tight-binding model discussed above can be understood from the transition at T_{s1}: The phase transition at T_{s1} is associated with a c-axis compression [1], which implies a change in crystal-field environment that drives n_{xz} and n_{yz} towards half-filling. In fact, this orbital-polarization shift is what triggers the band-Mott insulating transition in Ca_2RuO_4 [4, 5]. Although the c-axis compression is ~ 40 times smaller in $Ca_3Ru_2O_7$, we expect the filling of the d_{xz}/d_{yz} orbitals to change. Finally, note that the Brillouin-zone folding discussed above couples states at (k_x, k_y) with states at $(k_x + 2\pi/a, k_y)$, opening a gap as discussed in the main text from a pure symmetry perspective.

A final comment to the additional Fermi surface sheet that is not observed in the experiment [gray sheet in Supplementary Fig. 5(a)]. The absence of this band in the experiment could relate to photoemission matrix element effects. Given the agreement in the estimated specific heat value, a more plausible explanation is that our tight-binding modelling is too simplistic and that electronic interaction would gap out the missing sheet.

[1] Y. Yoshida, S.-I. Ikeda, H. Matsuhata, N. Shirakawa, C. H. Lee, and S. Katano, Phys. Rev. B **72**, 054412 (2005).
[2] D. J. Singh and S. Auluck, Phys. Rev. Lett. **96**, 097203 (2006).
[3] A. Georges, L. de' Medici, and J. Mravlje, Annu. Rev. Condens. Matter Phys **4**, 137 (2013).
[4] O. Friedt, M. Braden, G. André, P. Adelmann, S. Nakatsuji, and Y. Maeno, Phys. Rev. B **63**, 174432 (2001).
[5] Q. Han and A. Millis, Phys. Rev. Lett. **121**, 067601 (2018).